PCCP

RSC Publishing

PAPER

Incorporation of clusters of titanium oxide in Beta zeolite structure by a new cold $TiCl_4$-plasma process: physicochemical properties and photocatalytic activity†

Cite this: *Phys. Chem. Chem. Phys.*, 2013, **15**, 16198

Mohamad El-Roz,*[a] Louwanda Lakiss,[a] Jaafar El Fallah,[a] Oleg I. Lebedev,[b] Frederic Thibault-Starzyk[a] and Valentin Valtchev[a]

Received 14th June 2013,
Accepted 23rd July 2013

DOI: 10.1039/c3cp52478g

www.rsc.org/pccp

A new post-synthetic approach, involving cold plasma treatment, was employed for the preparation of TiO_2–Beta zeolite. Zeolite Beta nanoparticles were first subjected to plasma induced deposition of $TiCl_y$ (with $y \leq 3$), which were further converted into TiO_x (with $x \leq 2$) upon O_2-plasma treatment. Different steps of the new elaborated plasma approach were monitored using *in situ* FTIR spectroscopy. D_2O isotopic exchange was used in order to shed light on the formation of Si–O–Ti bonds induced by $TiCl_4$-plasma followed by O_2-plasma treatments. The obtained TiO_2–Beta materials were studied by a set of complementary characterization techniques including FTIR, TEM, SEM-EDS, XRD, N_2 sorption, NMR and UV-Vis. The silanol content and the acidic properties of TiO_2–Beta composites were also studied. The elaborated materials were tested as photocatalysts for methanol photooxidation in the gas phase. TiO_2–Beta presents a methanol photooxidation rate 8 times higher than a conventional P25-TiO_2 catalyst under UV irradiation.

Introduction

Over the last few years photocatalytic processes using titanium dioxide (TiO_2) as a photocatalyst have attracted special interest due to their numerous applications in water and air purification.[1–6] Because of its high activity and stability, low cost and non-toxic nature, titanium dioxide is considered as a very promising photocatalyst. When exposed to light in the presence of oxygen, it produces highly oxidative radical species that successfully oxidize most of the organic pollutants present in air and water into inert ultimate products such as CO_2 and H_2O.

Despite these valuable properties, the use of TiO_2 for industrial purposes remains limited due to the photocharge recombination[7] and adsorption–desorption processes of the reactants and reaction products.[8] It has also been reported that particle size distribution and dispersion of titanium dioxide particles have a direct impact on the efficiency of the catalyst. In this context, research studies focused mostly on the deposition of titanium dioxide onto different types of support not only to respond to the needs of highly dispersed TiO_2 nanostructures but also to exploit the adsorption properties of supports that might improve the photocatalytic activity. Several groups reported the preparation of TiO_2 supported onto different types of adsorbents such as fiber glass,[9,10] natural fiber,[11] activated charcoal,[12,13] alumina, silica or zeolite materials.[14–20] Among these supports, zeolites were found to be the ideal candidate due to their high specific surface area and micropore channels that provide confined space for stereoselective reactions. In addition, the physicochemical properties of zeolitic materials can be easily modified either by *in situ* or by post-synthesis methods. They are also eco-friendly and their tunable hydrophobic–hydrophilic character provides selective exclusion of undesired molecules or ions.[21,22] Recent studies have demonstrated the promising photocatalytic efficiency of TiO_2–zeolite composites[17,23–25] and interesting photovoltaic applications of clusters of titanium dioxide encapsulated within zeolites.[26]

TiO_2–zeolite supported photocatalysts can be prepared using different methods that are classified into three main groups: (i) solid state dispersion methods (SSD) or mechanical mixing;[17,27–29] (ii) post-synthetic approaches such as dealumination, followed by

[a] *Laboratoire Catalyse et Spectrochimie, Université de Caen Basse-Normandie, ENSICAEN CNRS, 6 bd Maréchal Juin, 14050 Caen, France. E-mail: mohamad.elroz@ensicaen.fr; Fax: +33 2 31 45 28 22; Tel: +33 2 31 46 27 32*

[b] *Laboratoire de Crystallographie et Science des Matériaux, Université de Caen Basse-Normandie, ENSICAEN CNRS, 6 bd Maréchal Juin, 14050 Caen, France*

† Electronic supplementary information (ESI) available: Cartographical analysis of Si and Ti in TiO_2–Beta and SSD TiO_2–Beta samples. Evolution of the IR spectra of Beta and TiO_2–Beta during Py desorption under vacuum at different temperatures. The bright field TEM image showing Beta zeolite–TiO_2 crystals and the corresponding ED pattern. See DOI: 10.1039/c3cp52478g

a vapor-thermal treatment using a TiO_2 precursor;[30] and (iii) *in situ* synthesis approaches where TiO_2 nanoparticles are anchored at the zeolite surface during the hydrothermal treatment.[14–16] Recently, several synthesis strategies have been reported for the preparation of Ti-Beta catalysts employing new templates and using fluoride media synthesis.[31,32]

Plasma treatment (thermal and non thermal) has also been used to prepare nanosized TiO_2 supported thin films (silica wafer, glass wafer...).[31–34] The most often employed TiO_2 precursor, for this treatment, is the titanium tetraisopropylat that is delivered in the gas phase comprising O_2, O_2/Ar, O_2/H_2O.[33–36] As known, during the plasma ionization of an oxygen-containing gas phase, oxidative species ($O_2^{\bullet -}$, O, O_3...) are generated. These species are able to oxidize the titanium precursor into crystalline TiO_2 that is deposited on the surface of the support. The formation of relatively large TiO_2 particles limits the preparation of efficient TiO_2–zeolite composites because of the difficulty incorporating TiO_2 in the zeolite pore system.

The present work reports the use of a modified cold $TiCl_4$-plasma approach that allows an efficient incorporation of clusters of titanium dioxide in the pore system and on the surface of zeolite-type materials. In contrast to the traditional plasma treatment described above, the present approach consists of the incorporation of atomic scale titanium species in zeolite channels. It is based on a direct-decomposition of the titanium vapor precursor ($TiCl_4$), by plasma ($TiCl_4$-plasma) in the absence of any other carrier gas, at low pressure (<0.5 mbar) and at relatively low temperature (<350 K). After the $TiCl_4$-plasma process, an O_2-plasma treatment is performed in order to oxidize the already deposited titanium species that are anchored to zeolite structure favoring the TiO_x formation by generating high oxidant species.[37] The elaborated TiO_x supported catalysts (TiO_2–Beta) were subjected to detailed characterization prior to be tested as photocatalysts for methanol photooxidation. For comparison, a reference sample prepared using the SSD method (TiO_2/Beta) was employed.

Experimental part

Synthesis and post synthesis treatment

Zeolite Beta synthesis. Nanosized Beta crystals (Beta) were synthesized from a colloidal precursor suspension having the following chemical composition: $0.35Na_2O : 4.5\ (TEA)_2O : 1Al_2O_3 : 30SiO_2 : 295H_2O$. The silica source for the preparation of the initial precursor suspension was freshly freeze-dried colloidal silica Ludox SM 30 (30 wt%). Aluminium isopropoxide (98%, Aldrich) was used as an alumina source and tetraethylammonium hydroxide (TEAOH, 20 wt% in water, Merck) as a structure-directing agent. These components were mixed under vigorous stirring for 15 min and aged on an orbital shaker at ambient temperature for 24 h prior to the hydrothermal treatment performed at 373 K for 8 days. The nanosized crystals resulting from the hydrothermal treatment of the colloidal suspension were purified by three step centrifugation (20 000 rpm, 60 min), decanting of the supernatant and redispersion in distilled water using an ultrasonic bath. The resulting suspension was freeze-dried to recover the sample in a powder form. The Beta zeolite crystals were then calcined to remove the organic template. The calcination process consisted of heating the sample from RT to 823 K at a heating rate of 1.75 K min^{-1}, kept at 823 K for 5 hours and then cooled down to room temperature in 5 hours.

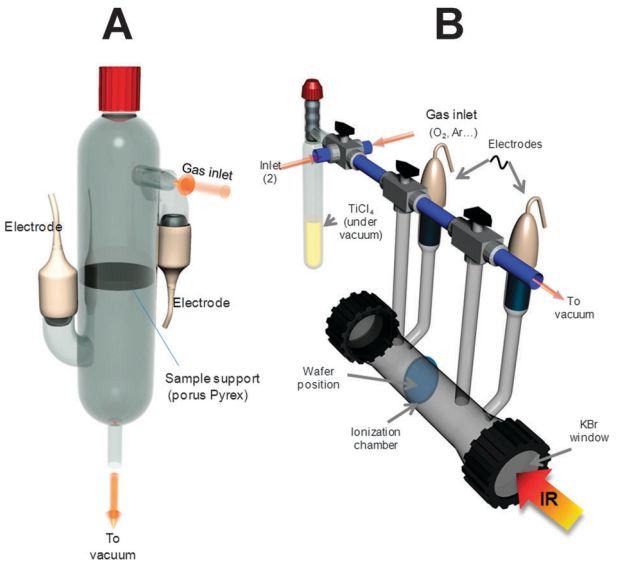

Scheme 1 Plasma (A) and *in situ* FTIR-plasma (B) reactors.

Preparation of TiO_2–Beta. The incorporation and encapsulation of titanium oxide in calcined Beta zeolite was performed using a plasma process in a Pyrex reactor (dielectric barrier discharge plasma with a 50 Hz sinusoidal power supply (2 kV)) (Scheme 1–A). After introducing the powder in the reactor, the system was evacuated until the pressure stabilizes at $\sim 10^{-2}$ mbar. Then $TiCl_4$ was introduced under continuous vacuum in order to reach an equilibrium pressure close to 0.5 mbar in order to purge the plasma reactor. The cold plasma was then turned on to decompose the $TiCl_4$ precursor in the absence of any other gas. It was maintained for about 5 to 10 seconds and then the valve of the $TiCl_4$ tube was closed in order to remove the excess of $TiCl_4$ and the different species formed during plasma. The process was repeated three times.

It should be noted that under our conditions the plasma was shut-off when the partial pressure of $TiCl_4$ exceeded 0.7 mbar. The $TiCl_4$-plasma treatment was followed by O_2-plasma treatment for more than 10 minutes (depending of the sample amount) at low pressure (3.5 mbar). During the experiments, the temperature increases due to the plasma process up to 393 K. The obtained material was named "TiO_2–Beta".

For comparison three types of samples were also investigated as references: a TiO_2 sample (P25 from Degussa), an initial zeolite Beta sample (used for the preparation of TiO_2–Beta), and a TiO_2–Beta sample (15/85 wt%) prepared by the Solid State Dispersion method using ethanol as solvent.

Characterization

In order to investigate the crystallinity and phase purity of the samples, calcined and treated Beta-type crystals were subjected

to X-ray diffraction (XRD) analysis using a PAN analytical (X-Pert Pro) diffractometer with a CuKα_1 source (λ = 0.15406 nm, 40 kV, 30 mA). The morphological features and the chemical analyses of the samples were studied using a Scanning Electron Microscope (SEM, Hitachi S3460) equipped with an energy dispersive spectroscopy (EDS, ThermoNoran) device. Beta and TiO_2–Beta materials were also characterized by transmission electron microscopy (TEM), including electron diffraction (ED), high resolution TEM (HRTEM) and energy dispersive X-ray (EDX) analysis, using a Technai G2 30UT microscope equipped with an EDAX X-ray microanalysis unit, operating at 300 kV and having 0.17 nm point resolution. The TEM samples were prepared by dispersing the powder onto a copper grid coated with a holey carbon film using ethanol as solvent. Low intensity beam conditions were applied for TEM measurements in order to minimize the degradation and amorphisation of the material under the electronic beam.

Nitrogen sorption measurements were carried out at 77 K on a Micromeritics ASAP 2020 after degassing at 423 K for 24 h. The surface areas were calculated using BET equation and the total pore volumes of the samples were estimated at a relative pressure of 0.99. The samples were also investigated using solid state NMR spectroscopy. MAS ^{29}Si and CP MAS ^{1}H $\rightarrow$ ^{29}Si NMR experiments were conducted at 300 K on a BRUKER ADVANCE 400 DSX spectrometer operating at 400 MHz–9.4 T for the ^{1}H Larmor frequency, and equipped with a BRUKER 4 mm ^{1}H/X solid-state CP MAS probe. A representative sample ($\sim$50 mg) was placed in a 4 mm zirconium rotor. The magic-angle spun at 14 kHz with pulse duration of 3.5 ms, contact time of 6 ms and relaxation time of 1 s. The number of scans was adjusted to ensure a signal-to-noise ratio of at least 1024. For MAS ^{27}Al NMR experiments, the spectra were recorded with a spinning speed of about 12 kHz. Chemical shifts were referenced to a 0.1 M $Al(NO_3)_3$ aqueous solution.

In order to investigate the surface modification of Beta-type zeolite during plasma treatment, *in situ* FTIR spectroscopy was performed on self-supporting wafers (20 mg/2 cm^2) placed in an *in situ* FTIR-plasma reactor (Scheme 1–B). First, the pellet was subjected to evacuation under vacuum in order to evacuate the atmospheric gas present in the ionization chamber and to remove water weakly adsorbed on the Beta surface. The first dose of $TiCl_4$ was introduced by opening the valve for $\sim$10 s to reach a pressure of $\sim$0.50 mbar under evacuation. This step allowed the evacuation of plasma reactor from the residual gases that could remained. The IR/plasma experiment was performed in the same order described above (see ''post synthesis treatment'' part) but for a shorter time due to the low amount of sample (pellet mass $\sim$20 mg). The IR spectra were collected in transmission mode on a Bruker Vertex 80v equipped with a cryogenic MCT detector (4 cm^{-1} resolution, 8 scans, and acquisition time $\sim$1.2 s).

The acidic properties of the resulting materials were investigated by IR using pyridine as a probe molecule. Powders were pressed ($\sim 10^7$ Pa) into self-supported discs (2 cm^2 area, $\sim$20 mg) and placed in an IR cell equipped with KBr windows. IR spectra were recorded using a Nicolet 6700 IR spectrometer equipped with a MCT detector and an extended-KBr beam splitter was used. Spectra were recorded in the 400–5500 cm^{-1} range at a resolution of 4 cm^{-1} and 128 scans were collected for each spectrum. A movable quartz sample holder allowed placing the self-supported discs in the infrared beam, for recording spectra, and moving it into a furnace at the top of the cell for thermal treatment. Pyridine (Py) adsorption was performed by introduction of doses inside the infrared cell containing the previously activated (under vacuum at 473 K for 5 h) self-supported discs of the samples. After introduction of each dose of Py, the Beta sample was heated at 473 K for 10 min to allow diffusion toward all accessible sites before recording the spectrum. Infrared spectra were recorded after Py saturation (1.33 mbar at equilibrium) followed by evacuation at 473 K to remove physisorbed species. In all experiments, analytical grade pyridine (Aldrich) was used after water trapping with molecular sieves of 3 Å. The decomposition of the massif into overlapping IR bands of adsorbed pyridine on acidic sites and the calculation of the IR band area have been performed using Omnic v8.2 software. The values were normalized for the same weight (20 mg) of pellets.

The accessible silanol sites were exchanged with heavy water vapor (D_2O) (10 mbar at equilibrium followed by an evacuation under vacuum at RT). This process was repeated 3 times in order to obtain a total H–D exchange of all accessible silanol sites. After exchange and evacuation, IR measurements were performed on a Nicolet 6700 IR spectrometer equipped with a MCT. Spectra were recorded at 4 cm^{-1} and 128 scans were co-added for each spectrum.

Photocatalytic tests

In order to test the photocatalytic activity of TiO_2–Beta materials, methanol photooxidation was performed. The TiO_2–Beta catalyst was pressed into self-supported wafers (2 cm^2, $m \sim 20$ mg) and put in the photocatalysis reactor. It was made of a stainless steel cylinder that carries a toroidal sample holder in its centre, where the catalyst self supporting wafer was placed. Tightness was obtained by Kalrez© O-rings, and the dead volume (typically defined as the residual space between each sample face and the windows) was reduced to about 0.4 ml by filling the empty space with KBr windows placed on each side of the sample holder. The photocatalytic system was connected to a flow set-up. Gases were introduced into the lines (heated at 333 K) by mass flow controllers. The system allows the two gas mixtures, so called ''activation'' and ''reaction'' flows, to be prepared and sent independently to the reactor cell. Gases were introduced to the sample by the 1/8″ OD pipe and collected on the opposite side of the sample holder. More details can be found in ref. 38–41. For this specific photocatalytic oxidation study, UV irradiation was carried out with a polychromatic light of a Xe–Hg lamp (LC8 spot light Hamamatsu, L10852, 200 W) with UV-intensity of about 6 mW cm^{-2} at λ = 366 nm. It was performed using a UV-light guide (A10014-50-0110) fixed at the entrance of a modified operando cell. The reaction temperature has been maintained at about 298 K.

The low partial pressure of methanol was established using a saturator at controlled temperature. The gas mixture composition

was then fixed at 1 vol% methanol and 20 vol% O_2 diluted in Ar and the total flow was adjusted to 25 cm^3 min^{-1}. The analysis of the outlet gases was performed by means of a Pfeiffer Omnistar mass spectrometer. P25-TiO_2 has been used as reference under the same conditions. Methanol conversion and CO_2-selectivity have been calculated using the m/z = 31 and m/z = 44 MS signals, respectively.[39]

Results and discussion

The as-synthesized zeolite Beta and the TiO_2–Beta composite obtained by plasma treatment are characterized by XRD (Fig. 1). Both display relatively broad Bragg reflections peaks characteristic of zeolite Beta structure, built of BEA and BEB polymorphs. No noticeable changes in the structure of the zeolite have been observed after plasma treatment. However, new broad peaks appear in the two theta regions 23–26° and 45–50°. They correspond to the TiO_2 anatase phase formed on the Beta surface.

The titanium content in the TiO_2–Beta sample was determined by EDS and ICP analysis. Fig. 2 presents the EDS spectrum of the TiO_2–Beta sample. It displays two peaks at 4.5 eV and 4.8 eV. According to the literature, these two peaks are assigned to $K_{\alpha 1}$ and K_β of titanium, respectively.[42] According to ICP results, the Si/Al ratio increases of about 5% after plasma treatment from Si/Al = 20.1 to 21.2. This result shows a partial extraction of Al from zeolite structure after plasma treatment. The amount of titanium species introduced is estimated to be 11 wt%. Besides, the cartography measurements performed on the composite TiO_2–Beta sample and the mechanical mixture TiO_2–Beta (15/85 wt%) show clearly the higher dispersion of Ti atoms in the TiO_2–Beta structure with respect to TiO_2/Beta (Fig. S1 in ESI†).

In order to determine the textural properties of calcined Beta, TiO_2–Beta, TiO_2/Beta and P25-TiO_2 samples, nitrogen sorption analysis was performed. Table 1 summarizes the most important characteristics of these materials. As shown in Fig. 3, all zeolite containing samples display a typical type I isotherm with

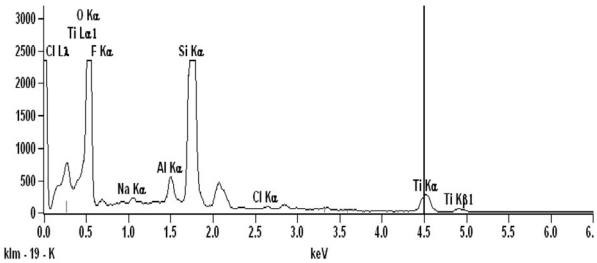

Fig. 2 EDS spectrum of the TiO_2–Beta sample.

Table 1 Specific surface areas and pore volumes of calcined Beta, TiO_2/Beta prepared using the SSD method and plasma treated TiO_2–Beta samples

	t_{plot}			
	S_{BET} (m^2 g^{-1})	V_{mic} (cm^3 g^{-1})	S_{meso} (m^2 g^{-1})	V_{meso} (cm^3 g^{-1})
Beta-calcined	634.0	0.26	100.7	0.48
TiO_2/Beta	570.1	0.22	93.0	0.41
TiO_2–Beta	421.9	0.17	83.9	0.39

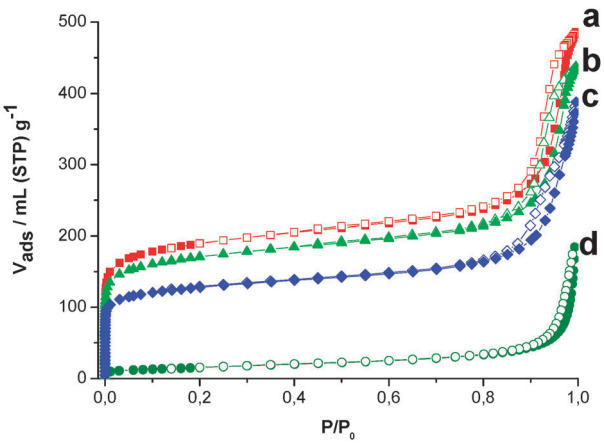

Fig. 3 Nitrogen adsorption (close symbol) and desorption (open symbol) isotherms of initial zeolite Beta (a), SSD prepared TiO_2/Beta (b), TiO_2–Beta (c) and P25-TiO_2 (d) samples.

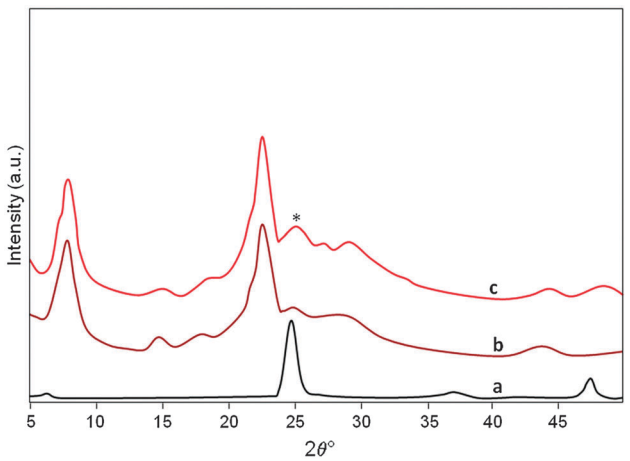

Fig. 1 XRD of pure anatase TiO_2 (a), Beta zeolite (b) and TiO_2–Beta (c) samples. Note: *peak assigned to the anatase phase.

hysteresis loops at high relative pressure. This latter is related to the textural porosity of aggregated nanosized zeolite crystals. The microporous volume was found to decrease in the following order Beta > TiO_2/Beta > TiO_2–Beta. The specific surface area decreased as well in the same order 635, 570 and 420 m^2 g^{-1} for Beta, TiO_2/Beta and TiO_2–Beta, respectively. The decreasing of the specific surface area and microporous volume of SSD prepared sample (TiO_2/Beta) is obviously due to the presence of 15 wt% bulk TiO_2. Although, the TiO_2–Beta sample contains a close amount (11%) of TiO_x ($x \leq 2$) species, a more pronounced decreasing of its microporous volume with respect to TiO_2/Beta was observed. This substantial difference in its microporous volume suggests that some amounts of TiO_x species introduced by plasma are located most probably in zeolite channels.

Fig. 4 shows the ^{29}Si MAS NMR spectra of the initial zeolite Beta and TiO_2–Beta samples. The two main signals, observed at

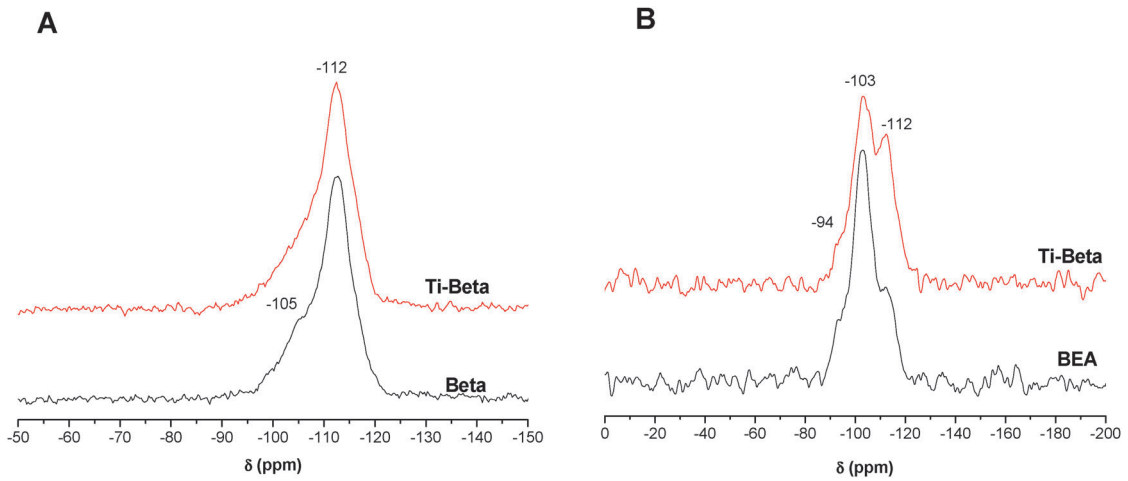

Fig. 4 ^{29}Si MAS (A) and CP MAS ^{1}H → ^{29}Si (B) NMR spectra of Beta and TiO_2–Beta samples.

−112 ppm and −105 ppm, are attributed to Q_4 ($(SiO)_4Si$) and Q_3 species ($(SiO)_3SiOH$), respectively. The signal assigned to the ($(SiO)_3SiOTi$) species, for TiO_2–Beta materials, appears at a higher field than that of ($(SiO)_4Si$) (Q_4), which explain the low resolution of Q_4–Q_3 signals for this sample.[43] As shown in Fig. 5, the ^{27}Al MAS NMR spectrum of TiO_2–Beta shows an increase of the signal at 0 ppm usually attributed to hexacoordinated aluminum species. Such a result reveals a partial dealumination of the structure after plasma treatment (in addition to the 5 wt% of alumina extracted from the structure and determined by ICP measurement). In addition, ^{1}H → ^{29}Si cross polarization experiments (Fig. 4B), that are more sensitive to Si–OH groups, show a spectacular increase of the Q_4/Q_3 ratio after the plasma incorporation of Ti. These results clearly point out a chemical interaction of Ti with the structure of zeolite and suggest the formation of the Si–O–Ti bond after $TiCl_4$-plasma treatment. This process is certainly complex and involves the interaction of chlorine ions with Al species followed by formation of Si–O–Ti linkages. Unfortunately, it is not possible to quantify the number of Aluminum sites substituted since hexacoordinated aluminium species are still present in the zeolite as shown by ^{27}Al mass NMR. However, according to ICP analysis this amount could be estimated to higher than 5%.

Fig. 6 includes the UV spectra of Beta-type material after calcination, the TiO_2–Beta sample, and P25-TiO_2. The initial Beta-type material exhibits a very low UV absorption. However, titanium-modified Beta material showed substantially different UV absorption characteristics, namely a blue shift of the UV spectra as compared to anatase and rutile forms of TiO_2. A broad band is observed between 200 and 350 nm, with a maximum centered at *ca.* 270 nm (Fig. 6). It is assigned to a charge transfer between oxygen and Ti atoms, simultaneously present in tetra-, penta- and hexacoordinated species. This band is broader than the one observed in TS-1 zeolite containing namely framework Ti.[44,45] A similar spectrum has been recorded for nanoclusters titanium oxide on silica.[46] Therefore, the UV spectra reveal the presence of clusters of titanium oxide in TiO_2–Beta zeolite.[44–46] This result shows also the presence of species with different coordination, including tetrahedral coordination that could be attributed to Ti atoms in the zeolite framework.

The bright-field TEM image (Fig. S3, ESI†) shows Beta zeolite nanocrystals with typical size of around 100 nm that are randomly surrounded by nanosized particles as it can be seen from the

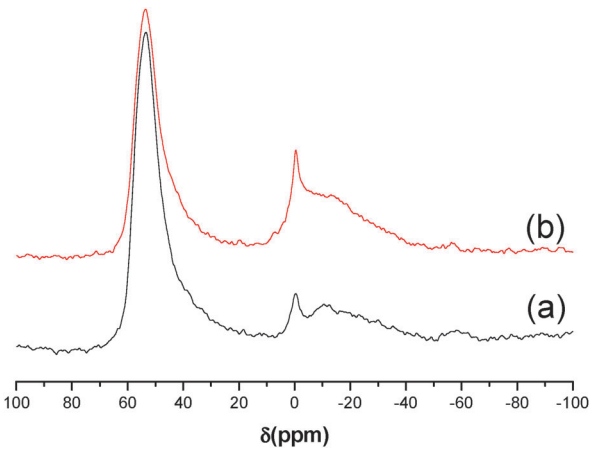

Fig. 5 ^{27}Al MAS NMR spectra of (a) Beta and (b) TiO_2–Beta samples.

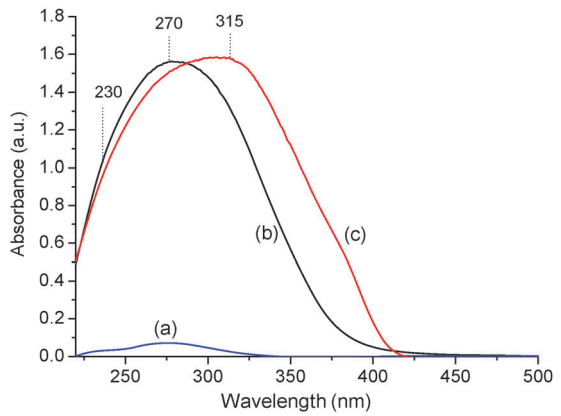

Fig. 6 DR UV-visible spectra of zeolite Beta (a), TiO_2–Beta (b) and P25-TiO_2 (c).

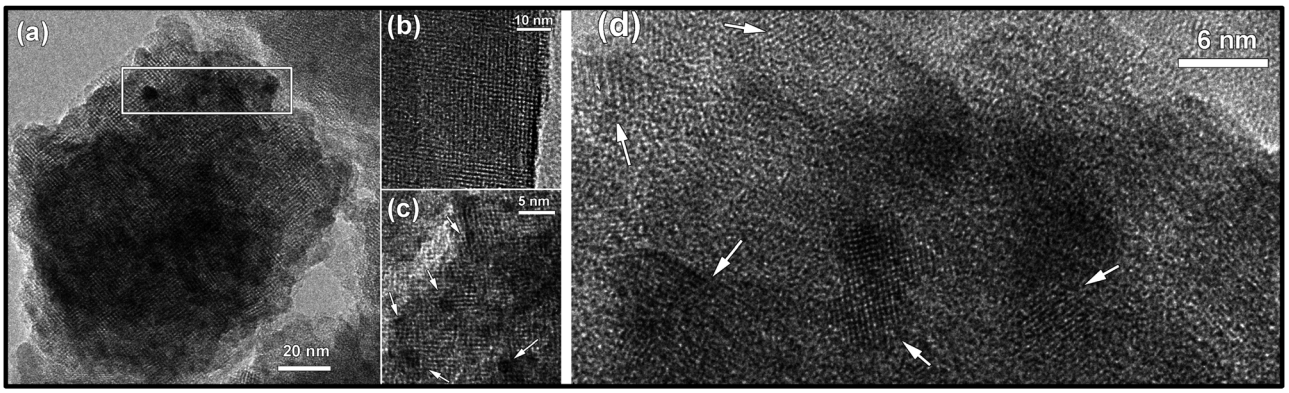

Fig. 7 (a) Bright field HRTEM image of the single TiO_2–Beta zeolite crystal; (b) bright field HRTEM image of parent Beta zeolite; (c) enlarged HRTEM image of TiO_2–Beta. The dark spots of Ti–O nanoparticles are pointed by white arrows; (d) enlarged image of the region marked in (a). The TiO_2 particles with range size between 4–6 nm are depicted by white arrows.

enlarged image of the inset. The inset ring ED pattern taken for this crystal shows evidence of coexistence of ultra small size TiO_2 nanoparticles and Beta zeolite crystals. In particular, together with the diffraction spots attributed to Beta zeolite, a faint ring is observed in the ED pattern. It corresponds to 3.5 Å, which is typical (011) spacing of TiO_2 anatase structure (ICSD 9852). This result is in agreement with that observed above by XRD.

High resolution TEM (HRTEM) gives more evidence and information on the structure and spatial distribution of TiO_2 nanoparticles. The bright field HRTEM image of the single Beta nanocrystal reported in Fig. 7 reveals a mixture of small and ultra small nanoparticles in the sample. The size and distribution of bigger particles is particularly clear in Fig. 7a and d. The small TiO_2 particles have a typical size of 4–6 nm and definitely located at the surface of Beta nanocrystals. The surface of zeolite nanocrystals is completely covered. Determining the structure and spatial distribution of clusters of TiO_2 by TEM is far from trivial due to the overlapping of the layer of big TiO_2 nanoparticles on the surface and the zeolite Beta matrix. However, the bright field HRTEM image in Fig. 7c shows very small particles with a scale size of 1–2 nm eventually spread, as dark spots, throughout the specimen. Unfortunately it is not possible to determine the spatial position of Ti–O particles within the Beta zeolite framework due to the two dimensional aspect of TEM images, and even by using electron tomography because of extremely small size, week contrast and complex structure of TiO_2–Beta material.[47] Nevertheless, the comparison of HRTEM images of pure Beta zeolite (Fig. 7b) and TiO_2–Beta crystals highlights two important points. The first point concerns the crystal structure: TiO_2–Beta zeolite crystals exhibit a disordered lattice (Fig. 7c) with respect to pure Beta zeolite crystals (Fig. 7b). The second point is that the Ti–O_x nanoparticles appearing as dark contrast spots (marked by white arrows in Fig. 7c) exhibit quite uniform size ($\sim$2 nm) and shape (square-like) distribution. As the Beta zeolite consists of cubically arranged pores, it is logical to assume that the nanoparticles should follow this arrangement if they are embedded within the structure framework. Thus according to these evidences, it is reasonable to conclude that clusters of titanium oxide are encapsulated within the Beta zeolite framework.

In situ FTIR-plasma results

The IR spectrum of the Beta zeolite sample displays two main narrow bands at 3740 cm^{-1} and 1630 cm^{-1} (Fig. 8), in addition to the characteristic structural vibration bands. These two bands correspond, respectively, to the ν(OH) of terminal silanol groups and to the $\delta(H_2O)$ of adsorbed water molecules.[48–50] The broad band appearing between 3700 and 2800 cm^{-1} is assigned to hydrogen bonded terminal silanol groups Si–OH with physisorbed water molecules.[48–50] The evolution of the IR spectra during plasma treatment and after each treatment step is reported in Fig. 8–A and B, respectively. First, the introduction of $TiCl_4$ leads to the disappearance of the band assigned to adsorbed water molecules in Beta zeolite. This is coupled with a decrease of the hydrogen bonding band related with the terminal silanol band. These changes in the IR spectra were assigned to the oxidation of $TiCl_4$ to $Ti(OH)_nCl_{(4-n)}$ ($n \leq 3$) in the presence of physisorbed water and to the formation of $SiOTi(OH)_mCl_{(3-m)}$ ($m \leq 3$) in the presence of terminal SiOH groups.[49] The total consumption of water molecules, traduced by the complete disappearance of the vibration band of water

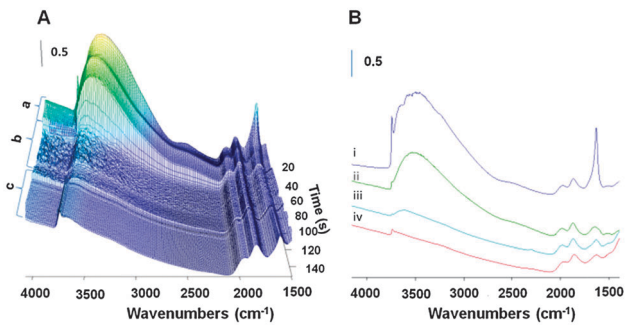

Fig. 8 (A) Evolution of zeolite Beta IR spectrum *vs.* the treatment time: during $TiCl_4$ introduction (a), during $TiCl_4$-plasma (b) and during O_2-plasma treatment (c). (B) IR spectra of Beta zeolite (i), after $TiCl_4$ introduction (ii), after $TiCl_4$-plasma (iii) and after O_2-plasma (iv) treatment.

at 1630 cm^{-1}, shows that all the accessible sites to water were also accessible to $TiCl_4$. The broad band of SiOH vibration, which is still present, is most probably a consequence of the hydrogen bonding between SiOH sites and the hydrolysed titanium precursor. When $TiCl_4$-plasma is turned on, a notable decrease of the SiOH bands is observed in the first few seconds. The observed changes are related to $TiCl_4$ decomposition and generation of active ions and/or radicals (*i.e.* $(TiCl_{4-n})^{m+}$, $Cl^{\bullet}$, Cl^{-}...) that favor Si–OH and TiOH condensation to form SiOTi and/or TiOHs condensation to form TiOTi bonds. This result is in agreement with the NMR results discussed above. The O_2-plasma treatment results in further condensation and oxidation of the reduced titanium species that could be present in the structure of TiO_x ($x \leq 2$). The arising of the narrow band at ~3740 cm^{-1} after O_2-plasma (Fig. 8B–iv) can be assigned to inaccessible silanol groups and/or to the formation of terminal TiOH groups after the condensation reaction (TiOH···TiOH···TiOH + oxydant species → TiOTiOTiOH + H_2O).

Silanol content in TiO_2–Beta and Beta samples

Fig. 9 presents the IR spectra of zeolite Beta nanocrystals and TiO_2–Beta samples in the SiOH vibration region after activation of the parent zeolite Beta samples at 623 K under vacuum for 1 h and after O_2-plasma treatment for TiO_2–Beta. The silanol contents have been determined using the normalized area of the ($\nu + \delta$) SiOH vibration band at 4570 cm^{-1} (inset of Fig. 8).[51] An important decrease of SiOH groups after $TiCl_4$-plasma followed by O_2-plasma treatment can be observed (Fig. 9, inset). The comparative study revealed that the relative silanol contents in Beta/TiO_2–Beta samples are equal to 2.4/1. This result unambiguously confirms that more than 50% of silanol defects disappear after $TiCl_4$-plasma treatment and proves that the extracted Aluminum species were substituted by Ti. The analysis has been repeated several times in order to verify the reproducibility of the result and to estimate the relative incertitude (±5%) on silanol ratio values.

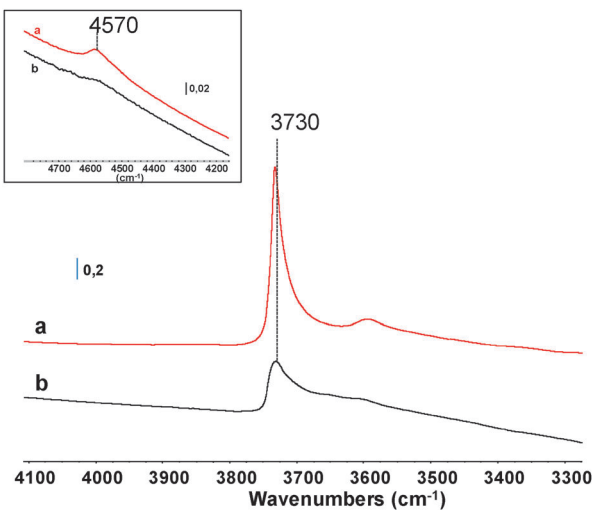

Fig. 9 IR spectra of the Beta sample after activation at 673 K under vacuum (a) and the TiO_2–Beta sample after plasma treatment in the OH vibration region (b). Spectra are normalized to the same weight of pellets.

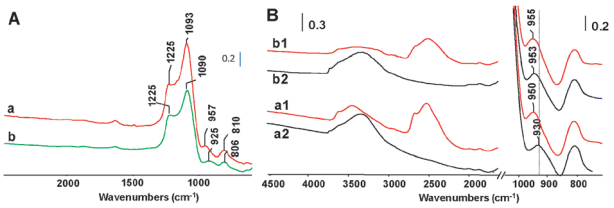

Fig. 10 (A) IR spectra of TiO_2–Beta (a) and calcined Beta (b) samples diluted in KBr (2 wt%). (B) IR spectra of TiO_2–Beta (a) and calcined Beta (b) samples diluted in KBr (5 wt%) before (1) and after (2) D_2O exchange.

Structural bands and isotopic exchange

In order to investigate the spectral region 600–1250 cm^{-1} corresponding to the intense structural bands of zeolite (Si–O and Al–O) the samples were studied after dilution with KBr. Fig. 10–A shows the IR spectra of TiO_2–Beta and Beta samples. The main structural vibration bands characteristic of zeolite-type material are observed at 1225, 1090 and 806 cm^{-1}. Another important and distinctive feature for TiO_2–Beta is observed at about 955 cm^{-1}. Although the assignment of this band is still in debate, the presence of this band after dehydration of samples under high-vacuum conditions is generally accepted as a solid proof for the incorporation of Ti into the framework.[43,52–55] This band is notably different from the one at 930 cm^{-1} that can be observed in zeolite Beta. The latter is assigned to the ν(Si–OH) vibrations. In order to shed more light on the origin of this band the two samples were subjected to an isotopic H–D exchange. After D_2O exchange, the IR spectra of TiO_2–Beta and Beta samples (Fig. 10–B) show a strong decrease of the bands in the ν(OH) (3750–3500 cm^{-1}) range with a concomitant formation of a ν(OD) band (2760–2600 cm^{-1}). Moreover a 20 cm^{-1} shift of the band at 930 cm^{-1} is also observed in the pure zeolite sample. The latter band is attributed to the H–D exchange of silanol groups.[56] A negligible shift, from 953 cm^1 to 955 cm^{-1} is observed in the case of plasma treated material. This result undoubtedly confirms the hypothesis of Si–O–Ti formation.

Acidic properties

Pyridine (Py) has been employed as a probe molecule to study the acidity of Beta, TiO_2–Beta, TiO_2/Beta and TiO_2 samples. Fig. 11 presents the recorded IR spectra of these samples after Py adsorption (Py desorption *vs.* temperature is presented in Fig. S2 and S3 in ESI†). The IR spectrum of zeolite Beta shows distinct bands at 1455, 1490, 1545, 1622 and 1637 cm^{-1}. In the range 1400–1700 cm^{-1}, chemically adsorbed pyridine was revealed by the usual set of bands: (i) at 1545 and 1637 cm^{-1} assigned to pyridinium ions (PyH^+), (ii) at 1455 and 1622 cm^{-1} related to Lewis bonded pyridine (PyL_1), and (iii) the superposition of signals of Lewis and Brønsted adsorbed species at 1490 cm^{-1}.[57–64] In the case of the TiO_2–Beta sample, the IR spectrum reveals two additional bands at 1448 cm^{-1} and 1608 cm^{-1}. According to the IR spectrum of the pure TiO_2 sample, these bands are assigned to the interaction of Py molecules with Lewis acid sites of titanium oxide nanoparticles incorporated in zeolite Beta. These bands are very weak in the case of TiO_2/Beta which is probably

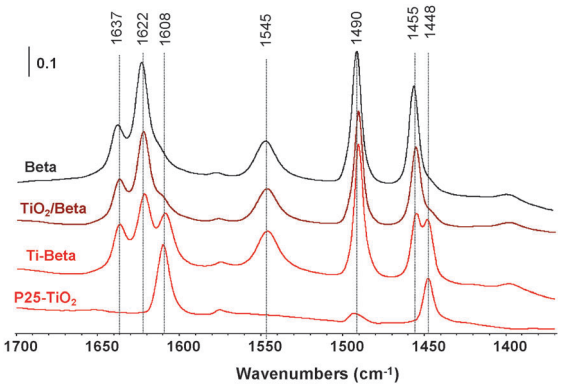

Fig. 11 IR spectra of zeolite Beta, SSD prepared TiO_2/Beta, TiO_2–Beta and P25-TiO_2 samples after pyridine adsorption (spectra before Py adsorption have been subtracted).

due to the low specific surface area of large TiO_2 aggregates. Thus, the high intensity of these two bands in TiO_2–Beta demonstrates the high dispersion and the cluster form of titanium dioxide (Fig. 11). These results are in a good agreement with the results obtained by EDS-SEM and HRTEM. On the other hand Py adsorption data do not point out dramatic modification in the acidic properties of Beta after plasma treatment.

TiO_2–Beta as a photocatalyst

In the present work, methanol photooxidation is used as a model reaction to study the photodegradation of volatile organic compounds (VOCs). No photocatalytic effect has been observed for the Beta zeolite sample. The conversion of methanol on TiO_2–Beta and P25-TiO_2 are presented in Fig. 12. Due to the different content of TiO_2 in the two samples, the methanol photodegradation rate (V_{MeOH}) has been calculated. It corresponds to the amount of methanol converted (vol_{MeOH}) per second per gram of TiO_2 ($g_{(TiO_2)}$). V_{MeOH} has been calculated with the following formula:

$$V_{MeOH} = [vol_{MeOH\text{-}converted}\ (ml)]/[m_{TiO_2}\ (g) \times time\ (s)](ml\ g^{-1}{}_{TiO_2}\ s^{-1}).$$

As shown in Fig. 12, a close methanol conversion has been observed using both materials. The photodegradation rates show that the V_{MeOH} value obtained using TiO_2–Beta is 8 times higher than that obtained using P25-TiO_2. This result could be assigned to the high dispersion and accessibility of titanium sites in TiO_2–Beta that compensate the low TiO_x content in this sample. The higher

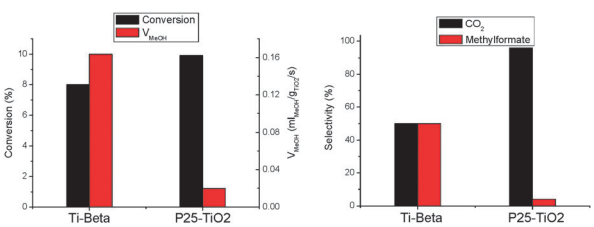

Fig. 12 Methanol conversion and CO_2-selectivity during methanol photoxidation on TiO_2–Beta and P25-TiO_2 photocatalysts *vs.* lamp intensity (%I_0). ([CH_3OH] = 1% in 20% of O_2 (vol%) diluted in Ar; flow = 25 cm^3 min^{-1}; T = 25 °C).

performance could also be related to the effect of zeolite structure in the separation of the electron–hole charges formed under irradiation, which improves the photocatalytic activity. In addition, the well known acidic properties of Beta zeolite could increase the adsorption of organic compound and hence the photoreactivity.

On the other hand, the selectivity of P25-TiO_2 and TiO_2–Beta photocatalysts was found to be different. More than 96% methanol photocombustion was obtained in the case of P25-TiO_2, whereas the formation of methyl formate contributed to ~50% of the methanol photooxidation on TiO_2–Beta catalysts. Thus the photocombustion reaction contributed to ~50% of the overall transformation on TiO_2–Beta. As mentioned before the difference in the catalytic activity of bulk TiO_2 is obviously related to the difference in active sites present in the two materials combined with the impact of zeolite structure in the case of TiO_2–Beta. These results allow investigating the use of TiO_2–Beta for green chemistry applications such as the synthesis of methyl formate from methanol using light energy.

Conclusions

Low temperature $TiCl_4$-plasma was used to incorporate highly dispersed titanium species in the structure of zeolite Beta. The ultimate material was subjected to comprehensive characterization using complementary methods (XRD, NMR, SEM-EDS, ICP, IR, UV-visible, HRTEM and N_2 sorption). More than 50% of the silanol defects present in the zeolite structure were disappeared after $TiCl_4$-plasma treatment. The formation of chemical bonds "Si–O–Ti" was also revealed. Indeed, the increase of the hexacoordinated aluminum species accompanied by a decrease of the silanol defects pointed out the insertion of Ti into the zeolite Beta framework. Pyridine adsorption showed higher dispersion of TiO_x in the TiO_2–Beta sample, which was found 10 times higher than that of TiO_2/Beta prepared using the SSD method. The properties of zeolite Beta were not significantly affected after plasma treatment. The parent and the treated samples showed close acidic and adsorption properties. The elaborated TiO_2–Beta composite was tested as a photocatalyst for methanol photooxidation. Plasma prepared TiO_2–Beta catalysts showed 8 times higher methanol photodegradation rates with respect to the reference P25-TiO_2 catalyst. This result demonstrated the potential of TiO_2–Beta photocatalysts for applications where the temperature is a critical parameter. It also showed that TiO_2–Beta could be used for water or air purification, green synthesis or photovoltaic application.

These results open the route to green photochemistry applications of Ti-containing zeolite catalysts prepared using the cold plasma method. Regarding the short time of the $TiCl_4$-plasma treatment, in addition to its efficiency, cost effective and eco-friendly, this method is particularly attractive for commercialization. Furthermore it does not require the use of solvents.

Notes and references

1 D. F. Ollis, E. Pelizzetti and N. Serpone, *Environ. Sci. Technol.*, 1991, **25**, 1522.
2 R. W. Matthews, *J. Phys. Chem.*, 1987, **91**, 3328.

3 D. Chatterjee and S. Dasgupta, *J. Photochem. Photobiol., C*, 2005, **6**, 186.
4 V. Ramaswamy, N. B. Jagtap, S. Vijayand, D. S. Bhange and P. S. Awati, *Mater. Res. Bull.*, 2008, **43**, 1145.
5 J. M. C. Robertson, P. K. J. Robertson and L. A. Lawton, *J. Photochem. Photobiol., A*, 2005, **175**, 51.
6 S. Romero-Vargas Castrillon and H. I. de Lasa, *Ind. Eng. Chem. Res.*, 2007, **46**, 5867.
7 B. J. Liu, T. Torimoto and H. Yoneyama, *J. Photochem. Photobiol., A*, 1998, **113**, 93.
8 J. A. Navio, G. Colon and J. M. Herrmann, *J. Photochem. Photobiol., A*, 1997, **108**, 179.
9 D. Robert, A. Piscoro, O. Heintz and J. V. Weber, *Catal. Today*, 1999, **54**, 291.
10 J. Medina-Valtierra, M. Sánchez-Cárdenas, C. Frausto-Reyes and S. Calixto, *J. Mex. Chem. Soc.*, 2006, **50**, 8.
11 M. El-Roz, Z. Haidar, L. Lakiss, J. Toufaily and F. Thibault-Starzyk, *RSC Adv.*, 2013, **3**, 3438.
12 H. Hou, H. Miyafuji and S. Saka, *J. Mater. Sci.*, 2006, **41**, 8295.
13 J. M. Herrmann, J. Matos, J. Disdier, C. Guillard, J. Laine, S. Malato and J. Blanco, *Catal. Today*, 1999, **54**, 255.
14 A. Corma, M. A. Camblor, P. Esteve, A. Martínez and J. Pérez-Pariente, *J. Catal.*, 1994, **145**, 151.
15 K. Lin, L. Wang, F. Meng, Z. Sun, Q. Yang, Y. Cui and D. Jiang, *J. Catal.*, 2005, **235**, 423.
16 M. Lafjah, F. Djafri, A. Bengueddach, N. Keller and V. Keller, *J. Hazard. Mater.*, 2011, **186**, 1218.
17 V. Durgakumari, M. Subrahmanyam, V. Subbaraok, A. Ratnamala, M. Noorjahan and K. Tanaka, *Appl. Catal., A*, 2002, **234**, 155.
18 S. Anandan and M. Yoon, *J. Photochem. Photobiol., C*, 2003, **4**, 5.
19 N. Takeda, T. Torimoto, S. Sampath, S. Kuwabata and H. Yoneyama, *J. Phys. Chem.*, 1995, **99**, 9986.
20 C. Anderson and A. Bard, *J. Phys. Chem. B*, 1997, **101**, 2611.
21 M. Mahalakshmi, S. Vishnu Priya, B. Arabindoo, M. Palanichamy and V. Murugesan, *J. Hazard. Mater.*, 2009, **161**, 336.
22 A. Corma, *Chem. Rev.*, 1997, **97**, 2373.
23 M. V. Phanikrishna Sharma, K. Lalitha, V. Durga Kumari and M. Subrahmanyam, *J. Hazard. Mater.*, 2008, **92**, 332.
24 M. V. Phanikrishna Sharma, K. Lalitha, V. Durga Kumari and M. Subrahmanyam, *J. Hazard. Mater.*, 2008, **160**, 568.
25 M. V. Phanikrishna Sharma, K. Lalitha, V. Durga Kumari and M. Subrahmanyam, *Chemosphere*, 2008, **72**, 644.
26 M. Álvaro, E. Carbonell, P. Atienzar and H. García, *Phys. Chem. Chem. Phys.*, 2006, **7**, 1996.
27 M. V. Shankar, K. K. Cheralathan, B. Arabindoo, M. Palanichamy and V. Murugesan, *J. Mol. Catal. A: Chem.*, 2004, **223**, 195.
28 M. P. Reddy, H. H. Phil and M. Subrahmanyam, *Catal. Lett.*, 2008, **123**, 56.
29 M. Takeuchi, J. Deguchi, M. Hidaka, S. Sakai, K. Woo, P. P. Choi, J. K. Park and M. Anpo, *Appl. Catal., B*, 2009, **89**, 406.
30 J.-P. Nogier, Y. Millot, P. P. Man, C. Méthivier, M. Che and S. Dzwigaj, *Catal. Lett.*, 2009, **130**, 588.
31 M. Sasidharana and A. Bhaumik, *Phys. Chem. Chem. Phys.*, 2011, **13**, 16282.
32 M. Sasidharana and A. Bhaumik, *J. Mol. Catal. A: Chem.*, 2010, **328**, 60.
33 N. G Kubala, C. Rowlette and C. A. Wolden, *J. Phys. Chem.*, 2009, **113**, 16307.
34 X. L. Zhang, L. H. Nie, Y. Xu, C. Shi, X. F. Yang and A. M. Zhu, *J. Phys. D: Appl. Phys.*, 2007, **40**, 1763.
35 C. Jiménz, D. D. Barros, A. Darraz, J. L. Deschanvers, L. Rapenne, P. Chaudouët, J. E Méndez, F. Weiss, M. Thomachot, T. Sindzingre, G. Berthomé and F. J. Ferrer, *Surf. Coat. Technol.*, 2007, **201**, 8971.
36 P. C. Rowlette and C. A. Wolden, *ACS Appl. Mater. Interfaces*, 2009, **11**, 2586.
37 M. El-Roz, L. Lakiss, V. Valtchev, S. Mintova and F. Thibault-Starzyk, *Microporous Mesoporous Mater.*, 2012, **158**, 148.
38 M. El Roz, P. Bazin and F. Thibault-Starzyk, *Catal. Today*, 2013, **205**, 111.
39 M. El-Roz, K. Monika, P. Cool and F. Thibault-Starzyk, *J. Phys. Chem. C*, 2012, **116**, 13252.
40 M. El-Roz, L. Lakiss, A. Vicente, K. Bozhilov, F. Thibault-Starzyk and V. Valtchev, *Chem. Sci.*, accepted.
41 M. El-Roz, P. Bazin and F. Thibault-Starzyk, *Catal. Today*, 2013, **205**, 111–119.
42 J. Yan, G. Gan, J. Du and J. Sun, *J. Phys.: Conf. Ser.*, 2009, **152**, 1.
43 W. Fan, R.-G. Duan, T. Yokoi, P. Wu, Y. Kubota and T. Tatsumi, *J. Am. Chem. Soc.*, 2008, **130**, 10150.
44 Y. Cheneviere, F. Chieux, V. Caps and A. Tuel, *J. Catal.*, 2010, **269**, 161.
45 O. I. Micic, M. Meglic, D. Lawless, D. K. Sharma and N. Serpone, *Langmuir*, 1990, **6**, 4403.
46 N. Serpone, D. Lawless and R. Khairutdinov, *J. Phys. Chem. B*, 1995, **99**, 16646.
47 S. Turner, O. I. Lebedev, F. Schröder, D. Esken, R. A. Fischer and G. Van Tendeloo, *Chem. Mater.*, 2008, **20**, 5622.
48 A. Vimont, F. Thibault-Starzyk and J. C. Lavalley, *J. Phys. Chem. B*, 2000, **104**, 286.
49 F. Thibault-Starzyk, A. Vimont and J.-P. Gilson, *Catal. Today*, 2001, **70**, 227.
50 A. Vimont, F. Thibault-Starzyk and J. C. Lavalley, *Stud. Surf. Sci. Catal.*, 2000, **130**, 2963.
51 J.-P. Gallas, J.-M. Goupil, A. Vimont, J.-C. Lavalley, B. Gil, G.-P. Gilson and O. Miserque, *Langmuir*, 2009, **25**, 5825.
52 G. Ricchiardi, A. Damin, S. Bordiga, C. Lamberti, G. Spano, F. Rivetti and A. Zecchina, *J. Am. Chem. Soc.*, 2001, **123**, 11409–11419.
53 D. R. C. Huybrechts, Ph. L. Buskens and P. A. Jacobs, *J. Mol. Catal.*, 1992, **71**, 129.

54 M. A. Camblor, A. Corma and J. Perez-Pariente, *J. Chem. Soc., Chem. Commun.*, 1993, 557.
55 M. R. Boccuti, K. M. Rao, A. Zecchina, G. Leofanti and G. Petrini, *Stud. Surf. Sci. Catal.*, 1989, **48**, 133.
56 G. Bellussi, A. Carati, G. M. Clerci, G. Maddellini and R. Millini, *J. Catal.*, 1992, **133**, 220.
57 A. Vimont, F. Thibault-Starzyk and J. C. Lavalley, *J. Phys. Chem. B*, 2000, **104**, 286.
58 F. R. J. Cannings, *Phys. Chem.*, 1968, **72**, 4691.
59 M. Lefrançois and G. J. Malbois, *J. Catal.*, 1971, **20**, 350.
60 R. Buzzoni, S. Bordiga, G. Ricchiardi, C. Lamberti, A. Zecchina and G. Bellussi, *Langmuir*, 1996, **12**, 930.
61 T. Barzetti, E. Selli, D. Moscotti and L. Forni, *J. Chem. Soc., Faraday Trans.*, 1996, **92**, 1401.
62 J. R. Sohn and E. H. Park, *J. Ind. Eng. Chem.*, 2000, **6**, 312.
63 A. Satsuma, A. Hattori, K. Mizutani, A. Furuta, A. Miyamoto, T. Hattori and Y. Murakami, *J. Phys. Chem.*, 1988, **92**, 6052.
64 J. R. Sohn, J. Kim, T.-D. Kwon and E. H. Park, *Langmuir*, 2002, **18**, 1666.